Multiple Nonvolatile Skyrmion States in Nanostructured Synthetic Antiferromagnetic Multilayers

Mangyuan Ma,[1] Wen Siang Lew,[2,*] and Fusheng Ma[1,†]

[1] *Jiangsu Key Laboratory of Opto-Electronic Technology, School of Physics and Technology, Nanjing Normal University, Nanjing 210046, China*

[2] *School of Physical and Mathematical Sciences, Nanyang Technological University, 21 Nanyang Link, Singapore 637371, Singapore*

Magnetic skyrmions have promising applications as nonvolatile memory for their particlelike and topological-protected features. The recently reported artificial skyrmion has shown a better prospect due to its controllable size and site. Here, we propose and experimentally demonstrate multiple nonvolatile skyrmion states in nanostructured synthetic antiferromagnetic $[Pt/Co]_4/Ru/[Co/Pt]_4$ multilayers at room temperature. Our magneto-optical Kerr effect measurements of major and minor reversal curves reveal that the skyrmion can exist at zero field with memristive behavior. Using the observed multiple skyrmion states, nonvolatile memory behavior is demonstrated. Our results provide evidence for the concept of skyrmion-based nonvolatile memory, i.e., skyrmion-based memristors and artificial synapses or neurons.

I. INTRODUCTION

The magnetic skyrmion, a topological nontrivial spin texture, has attracted extensive attention in recent years [1–5]. Considering its advantages of nanoscale size [6–8], particlelike features [9–11], topological stability [12–15], and magneto-electric properties [16–20], the skyrmion is expected to be a promising alternative as an information carrier in future functional spintronic devices, such as multilevel memories [21,22], nano-oscillators [23,24], and neuromorphic computing [25–29]. The skyrmion was discovered early in noncentrosymmetric *B*-20 bulk magnets with the assistance of an external field at low temperature [30]. To improve the feasibility of skyrmion-based spintronic devices, material systems that can host skyrmions at room temperature have been successively studied [31–36]. Ferromagnet-heavy-metal (FM-HM) multilayers are the mainstream skyrmion platform because of its compatibility with complementary metal oxide semiconductor manufacturing technology [37–41]. However, the stable existence of a skyrmion in FM-HM multilayers usually needs a large interfacial Dzyaloshinskii-Moriya interaction (DMI) and the assistance of an external field [42]. Furthermore, the skyrmions in continuous FM-HM multilayers nucleate spontaneously, and the size and nucleation sites are both uncontrollable [43]. To overcome these

obstacles, artificial skyrmions with higher controllability and lower conditions for existence (even without the DMI and external field) have become a research highlight [43–49]. So far, several nucleation mechanisms of artificial skyrmions are reported, such as an imprinting vortex [44,45], adding an integrated bias magnet [46], and irradiating with focused light [47,48]. In addition, nanostructured synthetic antiferromagnetic (SAF) multilayers are also a promising platform for hosting artificial skyrmions that are stabilized by the antiferromagnetic (AFM) interlayer exchange coupling (IEC) between the top nanostructures and bottom continuous ferromagnetic layer. Previous studies verified the ordered nucleation and stable existence of artificial skyrmions in nanostructured $[Pt/Co]_N/Ru/[Co/Pt]_4$ ($N = 2$, 4) multilayers [43,49]. The potential applications of these artificial skyrmions as functional spintronic devices are still rarely studied.

Recently, skyrmion-based racetrack memory devices were widely proposed, in which the binary data "0" or "1" are encoded by the skyrmion's nucleation and annihilation [50–53]. However, a transverse deflection of skyrmions due to the skyrmion Hall effect may lead to pinning or data loss. To improve data storage security and recoverability, the nonvolatile manipulation of skyrmions is necessary [21,54,55]. Here, we propose a scheme for the nonvolatile manipulation of skyrmion states in nanostructured $[Pt/Co]_4/Ru/[Co/Pt]_4$ multilayers. From the magneto-optical Kerr effect (MOKE) measured reversal curves [56] with different reversal fields, H_{R0} and H_{Rn} ($n = 1, 2, 3\ldots$),

it is found that the magnetization can be continuously modulated when H_{R0} is selected at the skyrmion state. Furthermore, multiple nonvolatile skyrmion states at zero field can be realized by the historical field process of "H_{R0}-H_{Rn}-H_{R0}." Our findings of realizing zero-field multiple nonvolatile skyrmion states can broaden the horizon of skyrmion-based functional spintronic devices.

II. RESULTS

Figure 1(a) shows a schematic and scanning electron microscopy (SEM) image of our nanostructured SAF multilayers. The top ferromagnetic [Co/Pt]$_4$ layers are etched into nanodots with diameter $d = 400$ nm and edge-to-edge spacing $S = 400$ nm. The 0.9-nm Ru layer makes the top [Co/Pt]$_4$ layers antiferromagnetically coupled with the bottom [Pt/Co]$_4$ layers [57,58]. The details of sample preparation can be found in Sec. I of the Supplemental Material [59]. Under the competition of a proper out-of-plane external field and AFM IEC between the top and bottom layers, a skyrmionlike spin texture, i.e., artificial skyrmion, is obtained under every nanodot in the bottom continuous [Pt/Co]$_4$ layers. In this case, the bottom continuous [Pt/Co]$_4$ layers would have a skyrmion-lattice-like configuration with an arrangement dictated by the arrangement of top nanodots [43,49]. Figure 1(b) shows the

descending branch of the MOKE-measured out-of-plane magnetization hysteresis (m_z-H_z) loop of the nanostructured [Pt/Co]$_4$/Ru/[Co/Pt]$_4$ multilayers (details of the MOKE measurement are given in Sec. II of the Supplemental Material [59]). Multistep switching reflects different magnetization states, which are labeled with numbers from 1 to 5. The bottom images in Fig. 1(b) schematically show the magnetization configurations of the five magnetization states: the positive saturation state, 1 (image 1); the antiferromagnetic state, 2 (image 2); the skyrmion state, 3 (image 3); the antiferromagnetic state, 4 (image 4); and the negative saturation state, 5 (image 5), as symmetrically studied in Refs. [43,49]. In addition, we also study the effect of different nanodot diameters, d, or edge-to-edge spacings, S, on the overall features of our sample; please see Sec. III of the Supplemental Material [59].

Considering the historical field manipulation of the skyrmion state in nanostructured [Pt/Co]$_4$/Ru/[Co/Pt]$_4$ multilayers, it is possible to use multiple skyrmion states at zero field as information bits instead of using the nucleation and annihilation of a single skyrmion. Here, we propose a scenario of multiple nonvolatile skyrmion states using memristive H_{R0}-H_{Rn}-H_{R0} reversal curves, as shown in Fig. 1(c). Since the ascending and descending branches of the m_z-H_z loop are symmetrical, here we consider only the descending branch. To promote the formation of
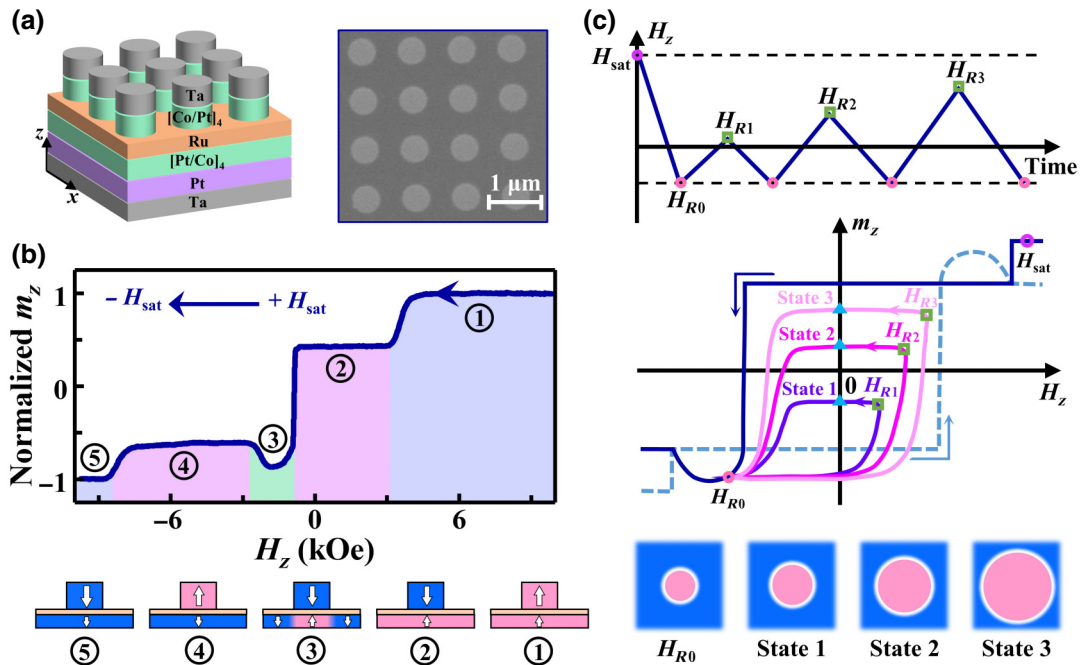

FIG. 1.   (a) Schematic of nanostructured SAF multilayers (left) and a SEM image of the fabricated sample (right). (b) Descending branch of MOKE-measured major m_z-H_z loop. Bottom images are the configurations of five different magnetization states: 1, positive saturation state; 2, antiferromagnetic state; 3, skyrmion state; 4, antiferromagnetic state; and 5, negative saturation state. Red (blue) colors indicate up (down) magnetization. (c) Proposed nonvolatile skyrmion states at zero field realized by controlling the reversal fields H_{R0} and H_{Rn} ($n = 1, 2, 3 \ldots$). Bottom images schematically present variations of the skyrmion in the continuous bottom layer of the nanostructured SAF structure.

skyrmion states at zero field, the value of reversal field H_{R0}, the starting point of the H_{R0}-H_{Rn}-H_{R0} reversal curve, has three possible choices, i.e., the skyrmion state (3), the antiferromagnetic state (4), and the negative saturation state (5), as shown in Fig. 1(b), while the reversal field H_{Rn} ($n = 1, 2, 3\ldots$) must be lower than the saturation field, H_{sat}. The realization of the nonvolatile skyrmion state can be understood from a single H_{R0}-H_{Rn}-H_{R0} reversal curve in Fig. 1(c) for H_{R0} selected at the skyrmion state. First, as H_z increases from H_{R0} to H_{Rn}, the skyrmion size will gradually increase to a maximum at H_{Rn}. Second, as H_z decreases from H_{Rn} to zero, the skyrmion size will be maintained, resulting in a nonvolatile skyrmion state at zero field. Finally, as H_z decreases from zero to H_{R0}, the skyrmion size will decrease to the initial size at H_{R0}. Therefore, different H_{Rn} will lead to different skyrmion states at zero field, as schematically shown in the bottom of Fig. 1(c). In the following, we experimentally study how

to realize multiple nonvolatile skyrmion states at zero field by choosing the values of H_{R0} and H_{Rn}. For ease of understanding, we present the magnetizations at H_{R0} and H_{Rn} as (H_{R0}, m_{z0}) and (H_{Rn}, m_{zn}), respectively.

First, we measure the H_{R0}-H_{Rn}-H_{R0} reversal curves with fixed H_{R0} selected in the skyrmion state and different H_{Rn}. Figures 2(a) and 2(b) show the measured H_{R0}-H_{Rn}-H_{R0} reversal curves with fixed $H_{R0} = -1.7$ kOe corresponding to the skyrmion state. For each reversal curve in Fig. 2(b), the out-of-plane magnetization, m_z, gradually increases from the minimum value, m_{z0}, to the maximum value, m_{zn}, and then back to m_{z0} during the external field history of H_{R0}-H_{Rn}-H_{R0}. Moreover, the evolution of m_z can indirectly reflect the continuous changes of skyrmion size, which highly depends on the competition between the negative external field and AFM IEC between top [Co/Pt]$_4$ nanodots and bottom continuous [Pt/Co]$_4$ layers. Interestingly, both the values of m_{z0} and m_{zn} at H_{R0} and H_{Rn} are
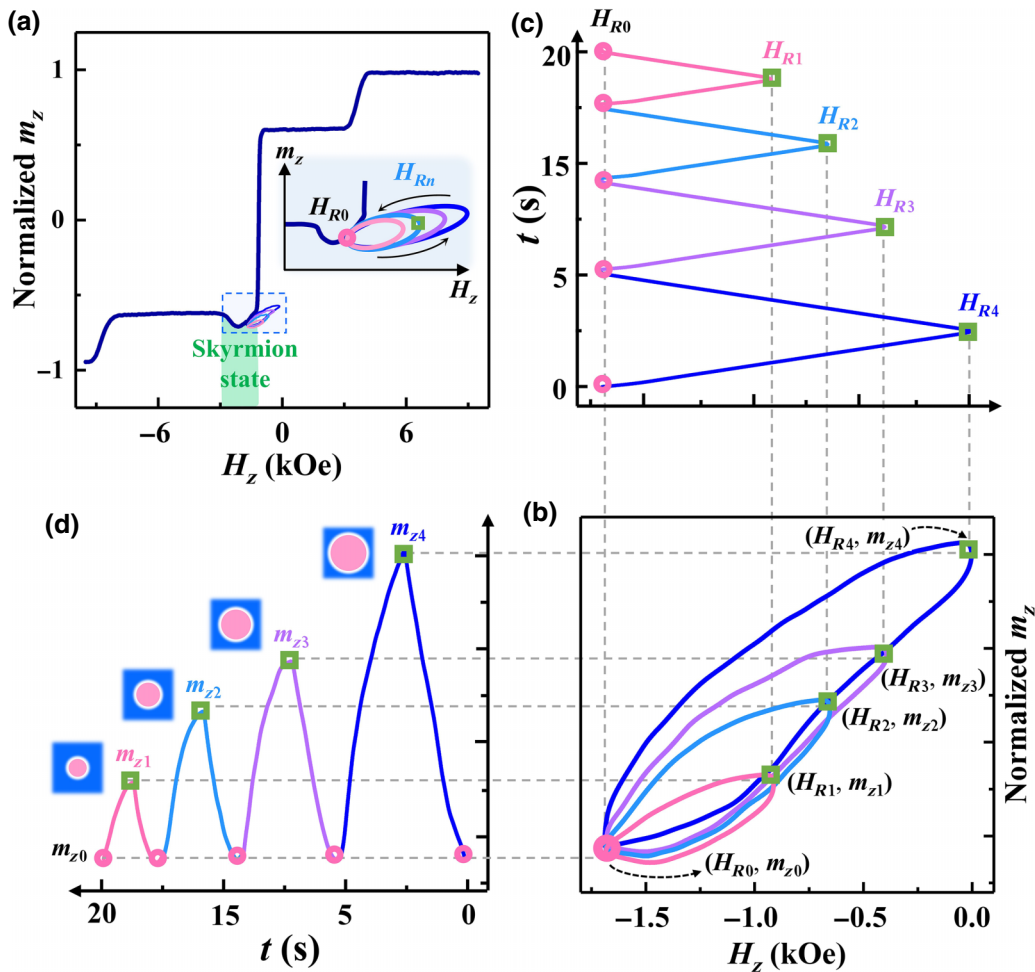

FIG. 2. (a) MOKE-measured descending branch of the major m_z-H_z loop and H_{R0}-H_{Rn}-H_{R0} reversal curves (H_{R0} selected at skyrmion state and H_{Rn} selected between H_{R0} and 0 Oe). Inset schematically shows the historical variation of m_z and H_z. (b) Magnified view of the measured H_{R0}-H_{Rn}-H_{R0} reversal curves indicated by the blue frame in (a). Temporal variation of external field H_z (c) and out-of-plane magnetization m_z (d) during the H_{R0}-H_{Rn}-H_{R0} reversal process in (b). Insets in (d) schematically indicate the sizes of skyrmions at various H_{Rn}.

repeatable, which indicates the robustness of the skyrmion states at H_{R0} and H_{Rn} against external-field history.

To more intuitively illustrate regulation of the external field on magnetization during the process of H_{R0}-H_{Rn}-H_{R0}, we plot the temporal variations of external field H_z and out-of-plane magnetization m_z, as shown in Figs. 2(c) and 2(d), respectively. The temporal evolution of m_z with H_z indicates that the external field can continuously control the magnetization, and hence, the skyrmion size can change continuously during the H_{R0}-H_{Rn}-H_{R0} process. Furthermore, the insets in Fig. 2(d) schematically show skyrmion variations at different H_{Rn}. Therefore, different skyrmion states at H_{Rn} can be obtained during the H_{R0}-H_{Rn}-H_{R0} process with different H_{Rn}. To realize our proposed scenario of multiple nonvolatile skyrmion states, the features of continuous manipulation of m_z by H_z and the stabilization of different skyrmion states at H_{Rn} are the key factors.

Second, we measure H_{R0}-H_{Rn}-H_{R0} reversal curves with fixed H_{R0} selected from the antiferromagnetic state and the negative saturation state. To find out the effect of H_{R0}, we compare the temporal variation of m_z during a two-circle reversal curve with three typical H_{R0}, as shown in Fig. 3(a), i.e., H_{R0}-H_{R1}-H_{R0}-H_{R2}-H_{R0}. Figures 3(b)–3(d) show the measured temporal variation of m_z with $H_{R0} = -1.7$ kOe (skyrmion state), -5.1 kOe (antiferromagnetic state), and -9.5 kOe (negative saturation state), respectively. For H_{R0} located in the skyrmion state, different reversal fields H_{R1} and H_{R2} lead to two different skyrmion states, corresponding to different magnetization values m_{z1} and m_{z2}, as shown in Fig. 3(b). For H_{R0} located in the antiferromagnetic state, the temporal variation of m_z manifests as a straight line, as shown in Fig. 3(c). This can be understood from the competition between the external field and the AFM IEC between the top [Co/Pt]$_4$ nanodots and bottom [Pt/Co]$_4$ layers. When the external field sweeps from H_{R0} to H_{Rn}, the AFM IEC is dominant, relative to the decreasing negative external field, which favors the existence of the antiferromagnetic state. Even upon reversing the external field from H_{Rn} to H_{R0}, the external field still cannot "defeat" the effect of AFM IEC. Therefore,
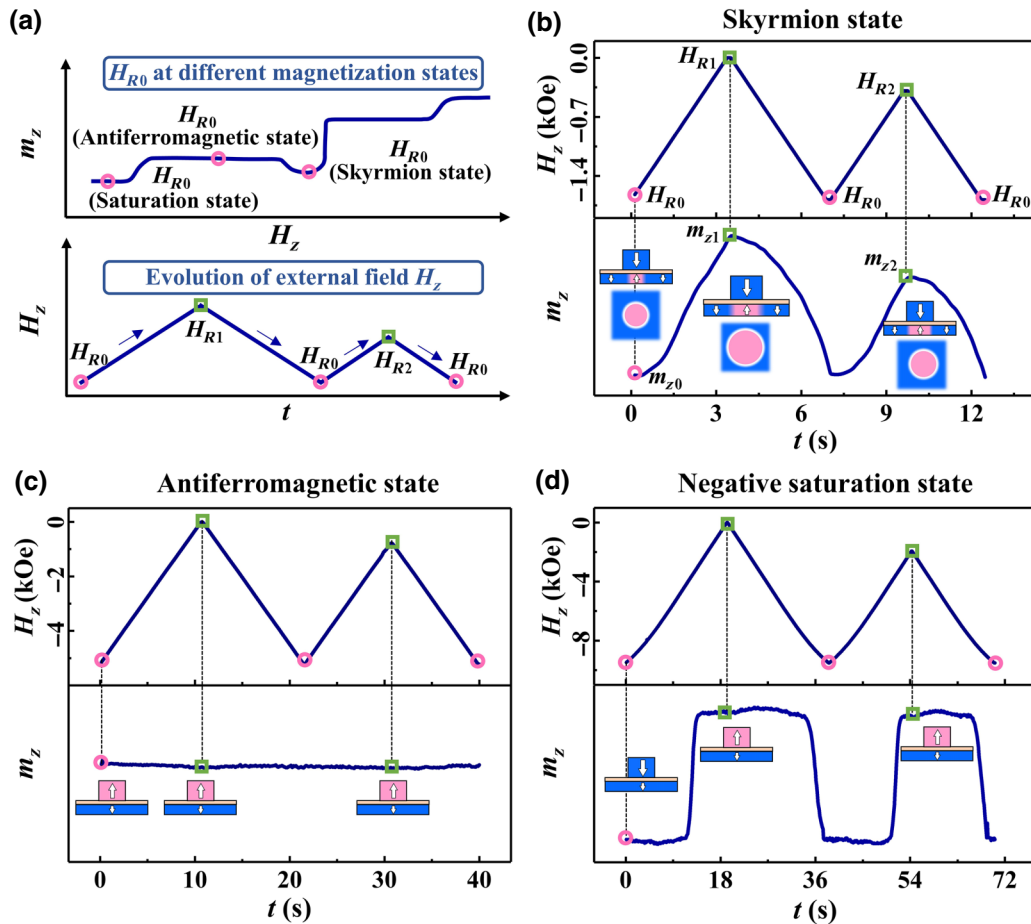

FIG. 3. (a) Scenario of selecting H_{R0} and H_{Rn}; typical values of H_{R0} located at different magnetization states (top) and temporal variation of H_z after H_{R0} is selected (bottom). MOKE-measured m_z variation corresponding to the temporal H_{R0}-H_{Rn}-H_{R0} process for H_{R0} selected at the skyrmion state (b), antiferromagnetic state (c), and negative saturation state (d). Insets schematically present the magnetization configurations at selected points with magnetization m_{z0} (pink circles) and m_{zn} (green squares).

the antiferromagnetic state cannot be changed during the H_{R0}-H_{R1}-H_{R0}-H_{R2}-H_{R0} process, along with unchanged m_z in Fig. 3(c). For H_{R0} located in the negative saturation state, the evolution of m_z with the external field is along the major m_z-H_z loop. When the external field sweeps from H_{R0} to H_{Rn}, the magnetization state transforms from the negative saturation state to the antiferromagnetic state. When the external field sweeps in reverse, the magnetization state also changes in reverse. So, the same magnetization states, i.e., the antiferromagnetic state, form at reversal fields H_{R1} and H_{R2}, as shown in Fig. 3(d). Therefore, we can conclude that the proper H_{R0} should be selected in the skyrmion state to realize the proposed scenario in Fig. 1(c).

To promote the emergence of multiple nonvolatile skyrmion states at zero field, we further measure the reversal curves with fixed H_{R0} at the skyrmion state and

$H_{Rn} > 0$, as shown in Figs. 4(a) and 4(b). The measured H_{R0}-H_{Rn}-H_{R0} reversal curves exhibit obvious memristive behavior and are consistent with that proposed in Fig. 1(c). It is worth noting that the nonvolatile behavior is obtained only by measuring the H_{R0}-H_{Rn}-H_{R0} reversal curves with $H_{Rn} > 0$. This is because the decreasing positive external field does not have the ability to reverse any negative magnetization of the bottom continuous magnetic layer during H_{Rn}-0 of the H_{R0}-H_{Rn}-H_{R0} reversal curves with $H_{Rn} > 0$ (skyrmion evolution processes with $H_{Rn} < 0$ and $H_{Rn} > 0$ are given in Sec. IV of the Supplemental Material [59]). We take the H_{R0}-H_{Rn}-H_{R0} reversal curve with $H_{R0} = -1.7$ kOe and $H_{Rn} = 0.56$ kOe in Fig. 4(b) as an example to discuss the stability of the corresponding nonvolatile skyrmion state at zero field (state 4). Figure 4(c) shows the MOKE-measured 0-H_{R0} curve (blue line) and
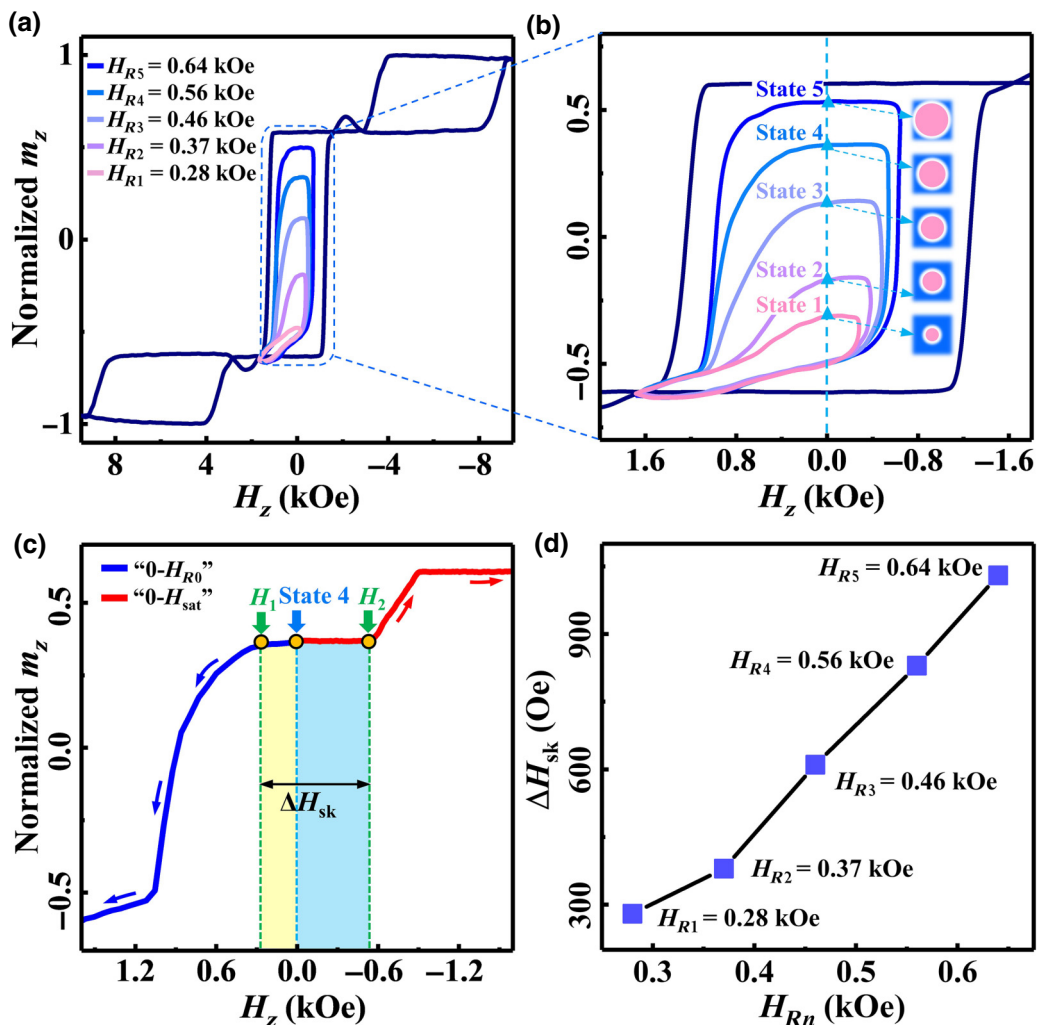

FIG. 4. (a) MOKE-measured major m_z-H_z loop and H_{R0}-H_{Rn}-H_{R0} reversal curves exhibiting nonvolatile behavior. (b) Magnified view of H_{R0}-H_{Rn}-H_{R0} reversal curves, as indicated by the blue frame in (a), and multiple nonvolatile states realized at zero field. Insets show the schematics of skyrmion states 1–5 at zero field. (c) MOKE-measured 0-H_{R0} curve (blue line) and the 0-H_{sat} curve (red line). Yellow and blue filled regions represent stable field ranges of the nonvolatile skyrmion state at zero field. (d) ΔH_{sk} of nonvolatile skyrmion states under different reversal fields H_{Rn}.

0-H_{sat} curve (red line) starting from state 4. State 4 can be maintained at both negative and positive external fields. H_1-0 (0-H_2) is the field range where state 4 can be stabilized in the negative (positive) field. The value of H_2 is similar to that of the reversal field $H_{Rn} = 0.56$ kOe. We define the total field range where state 4 can exist stably as ΔH_{sk} ($\Delta H_{sk} = H_2 - H_1$), $\Delta H_{sk} \approx 800$ Oe. This large ΔH_{sk} indicates that the nonvolatile skyrmion state in our system is robust to external fields. We also estimate ΔH_{sk} of different nonvolatile skyrmion states with different reversal fields H_{Rn}. The value of ΔH_{sk} increases from 280 to 1030 Oe with increasing H_{Rn} from 0.28 to 0.64 kOe, as shown in Fig. 4(d).

We also simulate several H_{R0}-H_{Rn}-H_{R0} reversal curves with different reversal fields H_{Rn} by using Mumax3 [60], as shown in Fig. 5(a) (details of micromagnetic simulation are given in Sec. V of the Supplemental Material [59]). For different field histories, reversal curves are different due to the magnetization hysteresis effect. With four different H_{Rn}, four nonvolatile skyrmion states (states 1–4) are obtained at zero field. The insets of Fig. 5(a) show simulated magnetization configurations of the bottom continuous magnetic layer at zero field, which indicate different skyrmion states at zero field. With the help of micromagnetic simulation, we also calculate the energies for different nonvolatile skyrmion states at zero field. The evolution of skyrmion states in our system mainly depends

on competition between the anisotropy energy, E_{an}; the exchange energy, E_{ex}; and the Zeeman energy, E_{Ze}. The demagnetization effect is included in E_{an} [61]. According to states 1–4 in Fig. 5(a), the total energy, E_{total}; E_{an}; and E_{ex} (E_{Ze} under zero field is negligible) are shown in Fig. 5(b). Different skyrmion states correspond to different E_{total}, and E_{total} has the same evolutionary trend as that of E_{an} and E_{ex}. Since E_{an} (10^{-15}) is an order of magnitude larger than E_{ex} (10^{-16}), we speculate that E_{an} is the main factor affecting the zero-field skyrmion state. Furthermore, it can be seen from previous studies that the skyrmion size increases with a decrease in $|E_{an}|$ [61,62]. Similarly in our work, the skyrmion size gradually increases with decreasing $|E_{an}|$ when H_{Rn} varies from 35 to 55 mT.

According to the reversal curves of Fig. 4(b), we experimentally propose a manipulation process of nonvolatile skyrmion states by a sequence of external fields, as shown in Fig. 6. The initialization, trigger, stabilization, and reset processes correspond to the sweeping of H_{sat}-H_{R0}, H_{R0}-H_{Rn}, H_{Rn}-0, and 0-H_{R0}, respectively. For the initialization process, the magnetization evolves along the major m_z-H_z loop, and the skyrmion state can approach H_{R0} ($H_{R0} = -1.7$ kOe) as an initial state. For the trigger process, different skyrmion states will emerge when the external field increases from H_{R0} to different H_{Rn} ($H_{R3} = 0.46$ kOe, $H_{R4} = 0.56$ kOe, $H_{R5} = 0.64$ kOe). For the stabilization process, the skyrmion state at H_{Rn} has a nonvolatile character
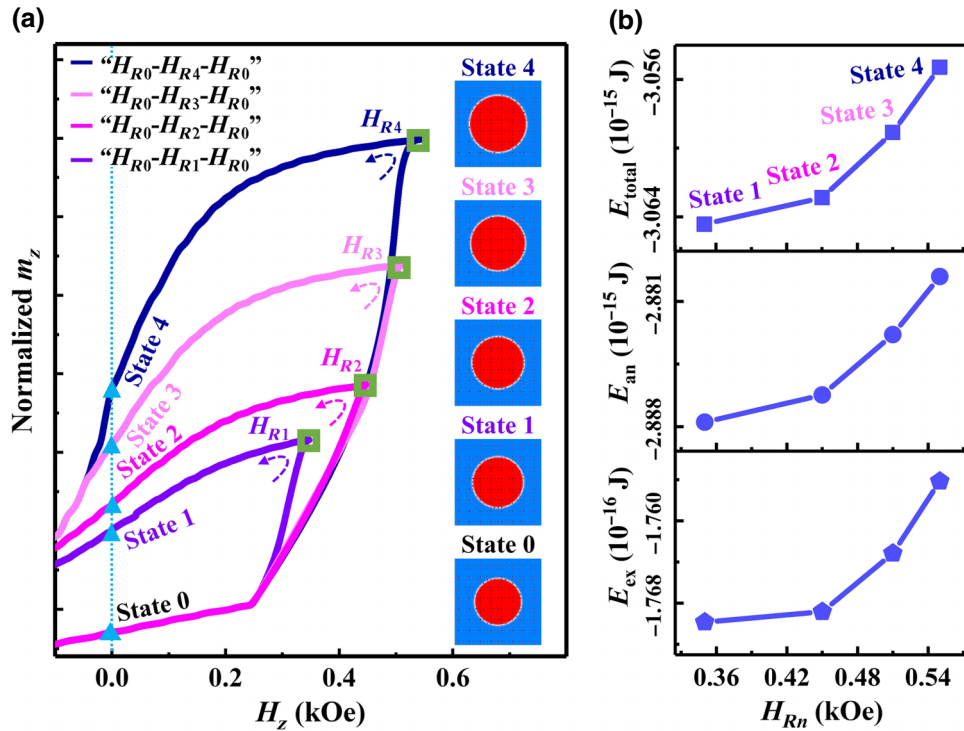

FIG. 5. (a) Simulated H_{R0}-H_{Rn}-H_{R0} reversal curves with different reversal fields H_{Rn}. Insets present simulated magnetization configurations for different skyrmion states at zero field. (b) Simulated E_{total}, E_{an}, and E_{ex} of states 1–4 at zero field, as marked in Fig. 5(a), with different reversal fields H_{Rn}.
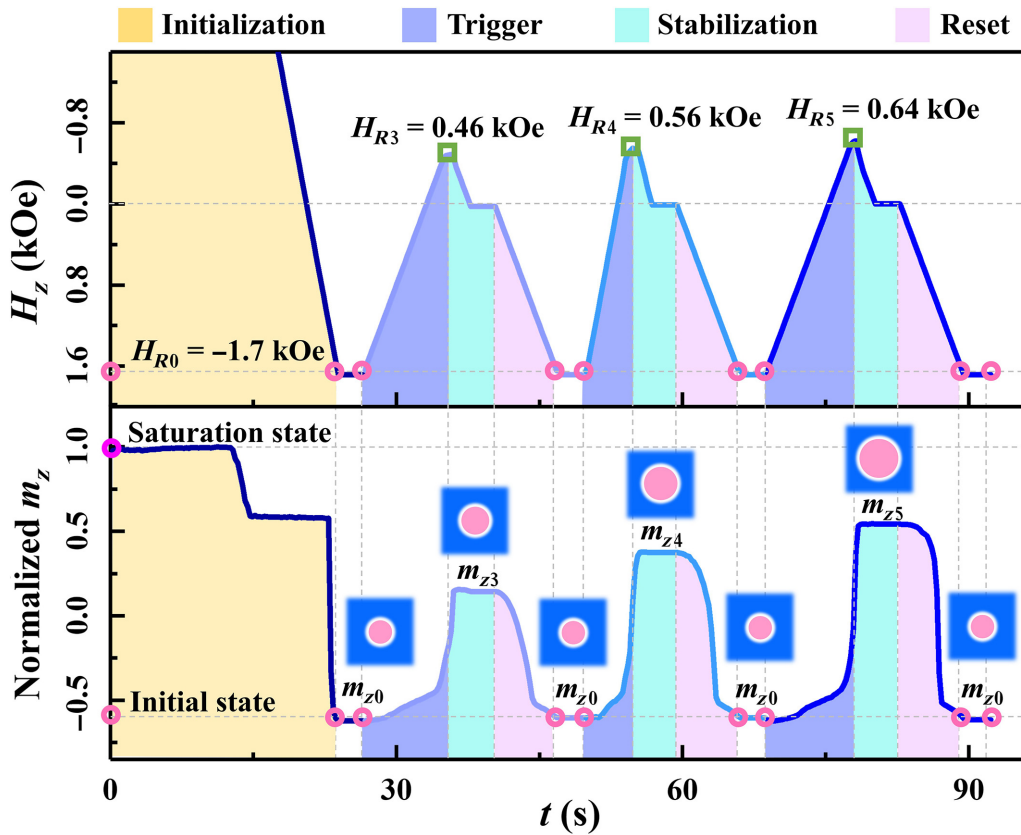
FIG. 6.   Nonvolatile behavior of memristive skyrmion states indicated by temporal variation of H_z (top) and m_z (bottom) during the MOKE measurements of multiple H_{R0}-H_{Rn}-H_{R0} processes.

when close the external field. For the reset process, the skyrmion state will return to the initial state when the external field decreases from 0 to H_{R0}. Because m_z at H_{R0} and H_{Rn} are both repeatable, the corresponding skyrmion states are determined under specific reversal fields H_{R0} and H_{Rn}, which guarantees the accuracy and security of the stored information.

III. CONCLUSION

We propose and experimentally demonstrate the existence of multiple nonvolatile skyrmion states in nanostructured SAF multilayers. Depending on the history of the external magnetic field, it is found that multiple skyrmion states with memristive sizes can be approached at zero field. Instead of using the nucleation and annihilation of skyrmions as information bits, we present the possibility of nonvolatile memory behavior by historical field manipulation of skyrmion sizes. Our findings show promise for the development of skyrmion-based memristive spintronic devices.

Here, we demonstrate the possibility of manipulating skyrmion magnetization as multiple nonvolatile states by using an external magnetic field as a stimulus. Actually, other ways can also be adopted, like an electric field

[54,63,64]. Recently, the voltage regulation of the continuous transition between large skyrmion bubbles and small skyrmions was achieved by tuning the Ruderman-Kittel-Kasuya-Yosida exchange coupling strength in nanostructured SAF multilayers using electric fields [65]. The zero-field nonvolatile skyrmion states are also obtained by tuning the remnant strain in a cylindrical magnetic-tunnel-junction device using electric fields [21]. Further work will be carried out to realize the electrical manipulation of skyrmion magnetization in a nanostructured SAF, as reported.

[1] T. H. R. Skyrme, A unified field theory of mesons and baryons, Nucl. Phys. **31**, 556 (1962).

[2] A. Bogdanov and A. Hubert, Thermodynamically stable magnetic vortex states in magnetic crystals, J. Magn. Magn. Mater. **138,** 255 (1994).

[3] A. Fert, N. Reyren, and V. Cros, Magnetic skyrmions: Advances in physics and potential applications, Nat. Rev. Mater. **2,** 17031 (2017).

[4] W. Jiang, G. Chen, K. Liu, J. Zang, S. G. E. te Velthuis, and A. Hoffmann, Skyrmions in magnetic multilayers, Phys. Rep. **704,** 1 (2017).

[5] K. Everschor-Sitte, J. Masell, R. M. Reeve, and M. Kläui, Perspective: Magnetic skyrmions − overview of recent progress in an active research field, J. Appl. Phys. **124,** 240901 (2018).

[6] K. Shibata, X. Z. Yu, T. Hara, D. Morikawa, N. Kanazawa, K. Kimoto, S. Ishiwata, Y. Matsui, and Y. Tokura, Towards control of the size and helicity of skyrmions in helimagnetic alloys by spin-orbit coupling, Nat. Nanotechnol. **8,** 723 (2013).

[7] N. Romming, A. Kubetzka, C. Hanneken, K. Von Bergmann, and R. Wiesendanger, Field-Dependent Size and Shape of Single Magnetic Skyrmions, Phys. Rev. Lett. **114,** 177203 (2015).

[8] Z. Qin, C. Jin, H. Xie, X. Li, Y. Wang, J. Cao, and Q. Liu, Size-tunable skyrmion bubbles in Ta/CoFeB/MgO multilayers, J. Phys. D: Appl. Phys. **51,** 425001 (2018).

[9] S. Seki, X. Z. Yu, S. Lshiwata, and Y. Tokura, Observation of skyrmions in a multiferroic material, Science **336,** 198 (2012).

[10] J. Tang, Y. Wu, W. Wang, L. Kong, B. Lv, W. Wei, J. Zang, M. Tian, and H. Du, Magnetic skyrmion bundles and their current-driven dynamics, Nat. Nanotechnol. **16,** 1086 (2021).

[11] C. D. Parmee, M. R. Dennis, and J. Ruostekoski, Optical excitations of skyrmions, knotted solitons, and defects in atoms, Commun. Phys. **5,** 54 (2022).

[12] S. Tewari, D. Belitz, and T. R. Kirkpatrick, Blue Quantum Fog: Chiral Condensation in Quantum Helimagnets, Phys. Rev. Lett. **96,** 047207 (2006).

[13] U. K. Rößler, A. N. Bogdanov, and C. Pfleiderer, Spontaneous skyrmion ground states in magnetic metals, Nature **442,** 797 (2006).

[14] B. Binz, A. Vishwanath, and V. Aji, Theory of the Helical Spin Crystal: A Candidate for the Partially Ordered State of MnSi, Phys. Rev. Lett. **96,** 207202 (2006).

[15] N. Nagaosa and Y. Tokura, Topological properties and dynamics of magnetic skyrmions, Nat. Nanotechnol. **8,** 899 (2013).

[16] N. Romming, C. Hanneken, M. Menzel, J. E. Bickel, B. Wolter, K. Von Bergmann, A. Kubetzka, and R. Wiesendanger, Writing and deleting single magnetic skyrmions, Science **341,** 636 (2013).

[17] J. Iwasaki, M. Mochizuki, and N. Nagaosa, Current-induced skyrmion dynamics in constricted geometries, Nat. Nanotechnol. **8,** 742 (2013).

[18] P. Milde, D. Köhler, J. Seidel, L. M. Eng, A. Bauer, A. Chacon, J. Kindervater, S. Mühlbauer, C. Pfleiderer, S. Buhrandt, et al., Unwinding of a skyrmion lattice by magnetic monopoles, Science **340,** 1076 (2013).

[19] A. Rosch, Skyrmions: Moving with the current, Nat. Nanotechnol. **8,** 160 (2013).

[20] A. Fert, V. Cros, and J. Sampaio, Skyrmions on the track, Nat. Nanotechnol. **8,** 152 (2013).

[21] S. Luo, N. Xu, Z. Guo, Y. Zhang, J. Hong, and L. You, Voltage-controlled skyrmion memristor for energy-efficient synapse applications, IEEE Electron Device Lett. **40,** 635 (2019).

[22] J. Grollier, D. Querlioz, K. Y. Camsari, K. Everschor-Sitte, S. Fukami, and M. Stiles, Neuromorphic spintronics, Nat. Electron. **3,** 360 (2020).

[23] S. Zhang, J. Wang, Q. Zheng, Q. Zhu, X. Liu, S. Chen, C. Jin, Q. Liu, C. Jia, and D. Xue, Current-induced magnetic skyrmions oscillator, New J. Phys. **17,** 023061 (2015).

[24] X. Liang, X. Zhang, J. Xia, M. Ezawa, Y. Zhao, G. Zhao, and Y. Zhou, A spiking neuron constructed by the skyrmion-based spin torque nano-oscillator, Appl. Phys. Lett. **116,** 122402 (2020).

[25] Y. Huang, W. Kang, X. Zhang, Y. Zhou, and W. Zhao, Magnetic skyrmion-based synaptic devices, Nanotechnology **28,** 08LY02 (2017).

[26] S. Li, W. Kang, Y. Huang, X. Zhang, Y. Zhou, and W. Zhao, Magnetic skyrmion-based artificial neuron device, Nanotechnology **28,** 31LT01 (2017).

[27] X. Chen, W. Kang, D. Zhu, X. Zhang, N. Lei, Y. Zhang, Y. Zhou, and W. Zhao, A compact skyrmionic leaky-integrate-fire spiking neuron device, Nanoscale **2018,** 6139 (2018).

[28] E. Raimondo, A. Giordano, A. Grimaldi, V. Puliafito, M. Carpentieri, Z. Zeng, R. Tomasello, and G. Finocchio, Reliability of neural networks based on spintronic neurons, IEEE Magn. Lett. **12,** 6102805 (2021).

[29] Y. Zhao, D. Guo, Z. Zeng, M. Shen, Y. Zhang, R. Tomasello, G. Finocchio, R. Wang, and S. Liang, Spin-orbit torque driven skyrmion motion under unconventional spin Hall effect, New J. Phys. **24,** 053053 (2022).

[30] S. Mühlbauer, B. Binz, F. Jonietz, C. Pfleiderer, A. Rosch, A. Neubauer, R. Georgii, and P. Böni, Skyrmion lattice in a chiral magnet, Science **323,** 915 (2009).

[31] X. Z. Yu, N. Kanazawa, Y. Onose, K. Kimoto, W. Z. Zhang, S. Ishiwata, Y. Matsui, and Y. Tokura, Near room-temperature formation of a skyrmion crystal in thin-films of the helimagnet FeGe, Nat. Mater. **10,** 106 (2011).

[32] W. Jiang, P. Upadhyaya, W. Zhang, G. Yu, M. B. Jungfleisch, F. Y. Fradin, J. E. Pearson, Y. Tserkovnyak, K. L. Wang, O. Heinonen, et al., Blowing magnetic skyrmion bubbles, Science **349,** 283 (2015).

[33] S. Woo, K. Litzius, B. Krüger, M. Y. Im, L. Caretta, K. Richter, M. Mann, A. Krone, R. M. Reeve, M. Weigand, et al., Observation of room-temperature magnetic skyrmions and their current-driven dynamics in ultrathin metallic ferromagnets, Nat. Mater. **15,** 501 (2016).

[34] C. Moreau-Luchaire, C. Moutafis, N. Reyren, J. Sampaio, C. A. F. Vaz, N. Van Horne, K. Bouzehouane, K. Garcia, C. Deranlot, P. Warnicke, et al., Additive interfacial chiral interaction in multilayers for stabilization of small individual skyrmions at room temperature, Nat. Nanotechnol. **11,** 444 (2016).

[35] O. Boulle, et al., Room-temperature chiral magnetic skyrmions in ultrathin magnetic nanostructures, Nat. Nanotechnol. **11,** 449 (2016).

[36] K. Karube, J. S. White, N. Reynolds, J. L. Gavilano, H. Oike, A. Kikkawa, F. Kagawa, Y. Tokunaga, H. M.

Rønnow, Y. Tokura, and Y. Taguchi, Robust metastable skyrmions and their triangular-square lattice structural transition in a high-temperature chiral magnet, Nat. Mater. **15,** 1237 (2016).

[37] J. E. Davies, O. Hellwig, E. E. Fullerton, G. Denbeaux, J. B. Kortright, and K. Liu, Magnetization reversal of Co/Pt multilayers: microscopic origin of high-field magnetic irreversibility, Phys. Rev. B **70,** 224434 (2004).

[38] A. Soumyanarayanan, M. Raju, A. L. G. Oyarce, A. K. C. Tan, M. Y. Im, A. P. Petrovic, P. Ho, K. H. Khoo, M. Tran, C. K. Gan, *et al.*, Tunable room-temperature magnetic skyrmions in Ir/Fe/Co/Pt multilayers, Nat. Mater. **16,** 898 (2017).

[39] J. B. Abugri, B. D. Clark, P. B. Visscher, J. Gong, and S. Gupta, MFM and first order reversal curve (FORC) study of switching mechanism in $Co_{25}Pd_{75}$ films, J. Appl. Phys. **126,** 013901 (2019).

[40] N. K. Duong, M. Raju, A. P. Petrović, R. Tomasello, G. Finocchio, and C. Panagopoulos, Stabilizing zero-field skyrmions in Ir/Fe/Co/Pt Thin film multilayers by magnetic history control, Appl. Phys. Lett. **114,** 072401 (2019).

[41] M. Ma, C. C. I. Ang, Y. Li, Z. Pan, W. Gan, W. S. Lew, and F. Ma, Enhancement of zero-field skyrmion density in $[Pt/Co/Fe/Ir]_2$ multilayers at room temperature by the first-order reversal curve, J. Appl. Phys. **127,** 223901 (2020).

[42] D. A. Gilbert, B. B. Maranville, A. L. Balk, B. J. Kirby, P. Fischer, D. T. Pierce, J. Unguris, J. A. Borchers, and K. Liu, Realization of ground-state artificial skyrmion lattices at room temperature, Nat. Commun. **6,** 8462 (2015).

[43] Y. Li, Q. Feng, S. Li, K. Huang, M. Ma, W. Gan, H. Zhou, X. Jin, X. Renshaw Wang, Y. Lu, *et al.*, An artificial skyrmion platform with robust tunability in synthetic antiferromagnetic multilayers, Adv. Funct. Mater. **30,** 1907140 (2020).

[44] L. Sun, R. X. Cao, B. F. Miao, Z. Feng, B. You, D. Wu, W. Zhang, A. Hu, and H. F. Ding, Creating an Artificial Two-Dimensional Skyrmion Crystal by Nanopatterning, Phys. Rev. Lett. **110,** 167201 (2013).

[45] J. Li, A. Tan, K. W. Moon, A. Doran, M. A. Marcus, A. T. Young, E. Arenholz, S. Ma, R. F. Yang, C. Hwang, and Z. Q. Qiu, Tailoring the topology of an artificial magnetic skyrmion, Nat. Commun. **5,** 4704 (2014).

[46] A. K. Nandy, N. S. Kiselev, and S. Blügel, Interlayer Exchange Coupling: A General Scheme Turning Chiral Magnets into Magnetic Multilayers Carrying Atomic-Scale Skyrmions, Phys. Rev. Lett. **116,** 177202 (2016).

[47] S. G. Je, P. Vallobra, T. Srivastava, J. C. Rojas-Sánchez, T. H. Pham, M. Hehn, G. Malinowski, C. Baraduc, S. Auffret, G. Gaudin, *et al.*, Creation of magnetic skyrmion bubble lattices by ultrafast laser in ultrathin films, Nano Lett. **18,** 7362 (2018).

[48] Y. Guang, *et al.*, Creating zero-field skyrmions in exchange-biased multilayers through x-ray illumination, Nat. Commun. **11,** 949 (2020).

[49] M. Ma, K. Huang, Y. Li, S. Li, Q. Feng, C. C. I. Ang, T. Jin, Y. Lu, Q. Lu, W. S. Lew, *et al.*, Nano-engineering the evolution of skyrmion crystal in synthetic antiferromagnets, Appl. Phys. Rev. **9,** 021404 (2022).

[50] J. Sampaio, V. Cros, S. Rohart, A. Thiaville, and A. Fert, Nucleation, stability and current-induced motion of isolated magnetic skyrmions in nanostructures, Nat. Nanotechnol. **8,** 839 (2013).

[51] R. Tomasello, E. Martinez, R. Zivieri, L. Torres, M. Carpentieri, and G. Finocchio, A strategy for the design of skyrmion racetrack memories, Sci. Rep. **4,** 6784 (2014).

[52] W. Kang, C. Zheng, Y. Huang, X. Zhang, W. Lv, Y. Zhou, and W. Zhao, Compact modeling and evaluation of magnetic skyrmion-based racetrack memory, IEEE Trans. Electron Devices **64,** 1060 (2017).

[53] D. Zhu, W. Kang, S. Li, Y. Huang, X. Zhang, Y. Zhou, and W. Zhao, Skyrmion racetrack memory with random information update/deletion/insertion, IEEE Trans. Electron Devices **65,** 87 (2018).

[54] Y. Wang, L. Wang, J. Xia, Z. Lai, G. Tian, X. Zhang, Z. Hou, X. Gao, W. Mi, C. Feng, *et al.*, Electric-field-driven non-volatile multi-state switching of individual skyrmions in a multiferroic heterostructure, Nat. Commun. **11,** 3577 (2020).

[55] Y. Fan, X. Han, X. Zhao, Y. Dong, Y. Chen, L. Bai, S. Yan, and Y. Tian, Programmable spin-orbit torque multistate memory and spin logic cell, ACS Nano **16,** 6878 (2022).

[56] Please refer to https://www.vertisis.com.sg/ for more details of the MagVision Kerr microscopy system.

[57] Y. Li, X. Jin, P. Pan, F. N. Tan, W. S. Lew, and F. Ma, Temperature-dependent interlayer exchange coupling strength in synthetic antiferromagnetic $[Pt/Co]_2$/Ru/[Co/Pt]_4$ multilayers, Chinese Phys. B **27,** 127502 (2018).

[58] P. X. Zhang, L. Y. Liao, G. Y. Shi, R. Q. Zhang, H. Q. Wu, Y. Y. Wang, F. Pan, and C. Song, Spin-orbit torque in a completely compensated synthetic antiferromagnet, Phys. Rev. B **97,** 214403 (2018).

[59] See the Supplemental Material at http://link.aps.org/supplemental/10.1103/PhysRevApplied.19.024029 for details of the experiments and micromagnetic simulation.

[60] A. Vansteenkiste, J. Leliaert, M. Dvornik, M. Helsen, F. Garcia-Sanchez, and B. Van Waeyenberge, The design and verification of MuMax3, AIP Adv. **4,** 107133 (2014).

[61] X. S. Wang, H. Y. Yuan, and X. R. Wang, A theory on skyrmion size, Commun. Phys. **1,** 31 (2018).

[62] H. Wu, X. Hu, K. Jing, and X. R. Wang, Size and profile of skyrmions in skyrmion crystals, Commun. Phys. **4,** 210 (2021).

[63] X. Wang, Q. Yang, L. Wang, Z. Zhou, T. Min, M. Liu, and N. X. Sun, *E*-Field control of the RKKY interaction in FeCoB/Ru/FeCoB/PMN-PT(011) multiferroic heterostructures, Adv. Mater. **30,** 1803612 (2018).

[64] Z. Hou, *et al.*, Controlled switching of the number of skyrmions in a magnetic nanodot by electric Fields, Adv. Mater. **34,** 2107908 (2022).

[65] Z. Yu, M. Shen, Z. Zeng, S. Liang, Y. Liu, M. Chen, Z. Zhang, Z. Lu, L. You, X. Yang, *et al.*, Voltage-controlled skyrmion-based nanodevices for neuromorphic computing using a synthetic antiferromagnet, Nanoscale Adv. **2,** 1309 (2020).